https://doi.org/10.5194/egusphere-2025-1596
Preprint. Discussion started: 29 April 2025

Technical note: Adaptably diagnosing O_3-NO_x-VOC sensitivity evolution with routine pollution and meteorological data

Minjuan Huang [1,2] *, Tengchao Liao [1,2]

[1] School of Atmospheric Sciences, Sun Yat-sen University, and Southern Marine Science and Engineering Guangdong Laboratory (Zhuhai), Zhuhai 519082, PR China
[2] Guangdong Provincial Observation and Research Station for Climate Environment and Air Quality Change in the Pearl River Estuary, Key Laboratory of Tropical Atmosphere-Ocean System (Sun Yat-sen University), Ministry of Education, Zhuhai, 519082, PR China

Correspondence to: Minjuan Huang (hminjuan@mail.sysu.edu.cn)

Abstract. Elucidating the evolving O_3-NO_x-VOC sensitivity in response to varying precursor emission trends is critical for mitigating the elevating ozone. Due to the complexities and resource constraints inherent in conventional methods, we developed an adaptable methodology addressing this issue through empirical parametric regression of routine data (O_3/NO_x/NO_2). The *log-Bragg3* model (Equation 3) performed best in globally characterizing the daytime ozone production (DPO_3)-NO_x (or NO_2) relation, including regions with severe $PM_{2.5}$ contamination where ozone formation is additionally influenced by aerosol-inhibited photochemical regime. Over 95% of these fits achieved statistical significance ($p<0.1$). This model provides parametric interpretations of ozone formation intensity (*d*), the associated chemical processes (*b*), and the O_3-NO_x-VOC sensitivity partition threshold (*e*). More vigorous photochemical reactions are implicated in the studied Chinese regions by higher values of parameters *b* (0.87-2.42) and *d* (34.72-54.78) relative to EU/US (*b*=0.26-0.57, *d*=9.97-31.45). Divergent temporal trends in parameter *b* further indicate fundamentally distinct evolutionary pathways in regional ozone chemistry between China and EU/US. Specific to MDA8-daytime hours, the Chinese city agglomerations were all diagnosed as being in the VOC-limited regime in both 2014 and 2019 on the regional scale, exhibiting significantly higher spatial predominance than the previous satellite-derived HCHO/NO_2 ratio inferences. The DPO_3-NO_2 pseudo-diagnosis constituted major uncertainty in spatiotemporal diagnosis, whereas the DPO_3-NO_x curve showed superior reliability. This methodology helps provide critical insights for formulating spatially differentiated precursor control policies.

https://doi.org/10.5194/egusphere-2025-1596
Preprint. Discussion started: 29 April 2025

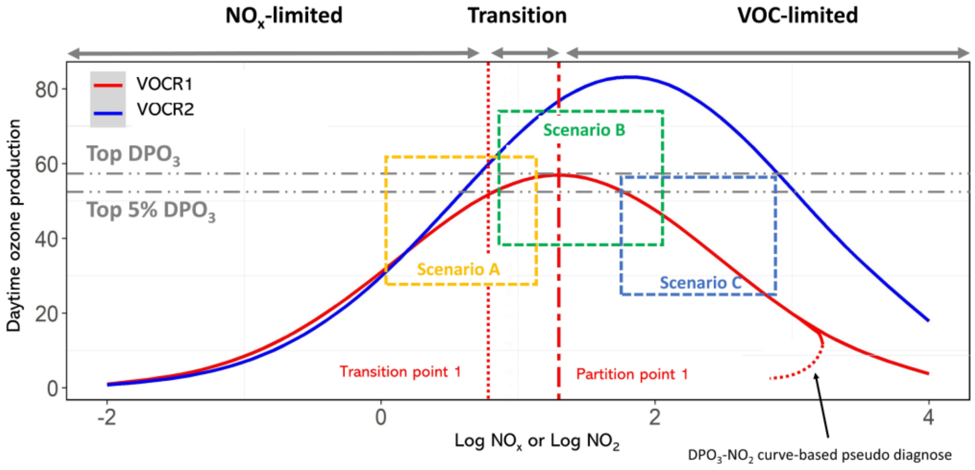

Graphical Abstract

1 Introduction

Tropospheric surface ozone (O_3) pollution harms human health and ecosystem (Collaborators, 2020; Ban et al., 2022; Agathokleous et al., 2023; Agathokleous et al., 2020; Feng et al., 2022). It is rapidly produced from the sunlight-driving oxidation of carbon monoxide (CO), methane (CH_4), and volatile organic compounds (VOCs) with the presence of nitrogen oxides (NO_x=NO+NO_2) (Atkinson, 2000; Wang et al., 2017; Li et al., 2018). Owing to shifting precursor emissions (Vazquez Santiago et al., 2024; Zhang et al., 2023), declining aerosol contamination (Li et al., 2019; Ivatt et al., 2022) and the warming environment (Schnell and Prather, 2017; Xiao et al., 2022b; Guo et al., 2023), the ozone level has increased in most urban areas worldwide (Wang et al., 2024; Vazquez Santiago et al., 2024). The O_3-NO_x-VOC sensitivity has likely evolved in response to the divergent trends in precursor emissions, and elucidating its long-term evolution is critical for effective ozone mitigation.

The current diagnosis methods, such as the Empirical Kinetic Modeling Approach (EKMA) isopleth plot and chemical indicators (e.g., H_2O_2/HNO_3, H_2O_2/NO_z, etc.), heavily rely on observation-based or numerical models, constrained by limited field data and computational demands. They are typically applied in case studies (Sillman and He, 2002; Sillman and West, 2009; Xue et al., 2014; Ou et al., 2016; Li et al., 2018). Although the satellite-derived HCHO/NO_2 ratio (FNR)-based method enables the regional scale long-term O_3-NO_x-VOC sensitivity diagnosis (Jin and Holloway, 2015; Ren et al., 2022; Wang et al., 2021; Zhang et al., 2024), its fixed daily sampling time restricts insights into other hours, and the sensitivity always varies over time (Sillman and West, 2009). These constraints highlight the necessity for more flexible and adaptable approaches.

For a specific VOC reactivity (VOCR), the daytime ozone production (DPO_3) exhibits a characteristic skewed curve when plotted against NO_x or NO_2, which is transformed from the EKMA plot (Pusede and Cohen, 2012; Romer et al., 2018; Nussbaumer and Cohen, 2020; Guo et al., 2023; Yang et al., 2021). As shown in the Graphical Abstract, ozone production rises with NO_x is insensitive to VOCR. Reducing NO_x is more effective than controlling VOCs to mitigate ozone. As NO_x increases. As NO_x rises, it reaches its maximum and became limited by both NO_x and VOCR. This indicates that controlling either or both precursors can effectively reduce ozone acceleration. With further NO_x increase, it grows with VOCR but declines with NO_x. Here, VOC control becomes the key for ozone mitigation, while NO_x reduction potentially leads to increase in ozone pollution.

Non-parametric smoothing of this curve using routine monitoring data has proven effective for OFR diagnosis in the Guangdong-Hong Kong-Macao Greater Bay Area, South China (Huang et al., 2025). However, two critical limitations persist: (1) a fixed smoothing configuration fails to exhibit robustness in fitting performance across spatiotemporal scales; (2) it fails to identify the NO_x-limited/transition boundary (red dotted line in Graphical Abstract), that requires parametric modelling. The DPO_3-NO_x (or NO_2) curve shows environmental stability (Guo et al., 2023), enabling the parametric characterization. Unlike the DPO_3-NO_x curve, the DPO_3-NO_2 curve may theoretically exhibit a bend in cases with extremely low DPO_3/NO_2 ratio

(Graphical Abstract) (Romer et al., 2018; Guo et al., 2023); in such cases, the ozone production decreases with NO_2, leading to a pseudo-diagnosis of the NO_x-limited regime under a realistic NO_x-saturated condition., which has been observed in Hong Kong (Huang et al., 2025).

Based on the above premises, the present study aims to: (1) verify the universality of DPO_3-NO_x (or NO_2) relation using routine monitoring networks (Section 3.1); (2) identify a globally capable empirical model for DPO_3-NO_x (or NO_2) characterization (Section 3.2); (3) compare the reliability between the DPO_3-NO_2 and DPO_3-NO_x curves in diagnosing O_3-NO_x-VOC sensitivity (Section 3.3); by utilizing the identified empirical model, (4) investigate the evolution of O_3-NO_x-VOC sensitivity for four Chinese city agglomerations (the Beijing−Tianjin−Hebei and surrounding (BTH) region, the Fenwei Plain (FWP), the Yangtze River Delta (YRD) region, and the Greater Bay Area (GBA)), the European Union (EU) and the United States (US), as well as discuss the model parametric implications and the primary uncertainty source for spatiotemporal diagnosis (Sections 3.4-3.6). We focused on the DPO_3−NO_x (or NO_2) relation and O_3-NO_x-VOC sensitivity within the MDA8-daytime hours, as MDA8 is one of the key air quality standard metrics around the world and usually employed to examine the ozone exposure attributable human health adverse effects.

2 Methodology

The DPO_3-NO_x (or NO_2) relation was regressed with the five-percentile-binned NO_x (or NO_2) concentrations (or logarithms) and their corresponding average DPO_3 levels. The DPO_3 was defined as the difference between the MDA8-daytime (7:00-19:00 Local Time (LT)) hourly ozone concentration and the ozone concentration at 6:00 LT. The non-parametric regression, smoothing a numerical series in local neighbourhood, was firstly utilized to reveal the intrinsic DPO_3-NO_x (or NO_2) relation. The parametric model validity was confirmed when its curve and partition point aligned well with the non-parametric results, demonstrating accurate ozone formation regime diagnosis.

2.1 Parametric models

A total of seven parametric models were individually applied to characterize the DPO_3-NO_x (or NO_2) relation, including the five-parameter *Beta* (Equation 1) and *logarithmic Beta* (*log-Beta*) (Equation 2) functions, the three- and four-parameter *logarithmic Bragg* (*log-Bragg3 and log-Bragg4*) functions (Equations 3-4), the three- and four-parameter *logarithmic Lorentz* (*log-Lorentz3 and log-Lorentz4*) functions (Equations 5-6), and the *logarithmic quadratic polynomial* (*log-Poly2*) function (Equation 7), where Y represents DPO_3 levels and X denotes NO_x (or NO_2) concentrations.

$$Y = d \times \left\{ \left(\frac{X - x_b}{x_o - x_b}\right) \times \left(\frac{x_c - X}{x_c - x_o}\right)^{\frac{x_c - x_o}{x_o - x_b}} \right\}^{b} \tag{1}$$

https://doi.org/10.5194/egusphere-2025-1596
Preprint. Discussion started: 29 April 2025

$$Y = d \times \left\{ \left(\frac{log(X) - log(x)_b}{log(x)_o - log(x)_b}\right) \times \left(\frac{log(x)_c - log(X)}{log(x)_c - log(x)_o}\right)^{\frac{log(x)_c - log(x)_o}{log(x)_o - log(x)_b}} \right\}^b \tag{2}$$

Specifically, in *Beta* and log-Beta models (Equations 1-2), parameter b determines curve shape; d represents the maximum fitted DPO_3; x_b (or $log(x)_b$) denotes the NO_x (or NO_2) concentration (or its logarithm) at peak DPO_3, serving as the partition point; x_o (or $log(x)_o$) and x_c (or $log(x)_c$) define the regression's lower and upper x-axis boundaries, respectively.

$$Y = d \times exp[-b \times (log(X) - e)^2] \tag{3}$$

$$Y = c + (d - c) \times exp[-b \times (log(X) - e)^2] \tag{4}$$

$$Y = \frac{d}{1 + b \times (log(X) - e)} \tag{5}$$

$$Y = c + \frac{d - c}{1 + b \times (log(X) - e)} \tag{6}$$

In *log-Bragg3*, *log-Bragg4*, *log-Lorentz3 and log-Lorentz4* models (Equations 3-6), b also relates to the curve width, determining the location of transition point; d also represents the maximum DPO_3 level; *e* is the maximum DPO_3 corresponding NO_x (or NO_2) level (the partition point); *c* is the non-zero lower asymptote.

$$Y = b_0 + b_1 \times log(X) + b_2 \times log(X)^2 \tag{7}$$

In *log-Poly2* model (Equation 7), the parameters b_0, b_1 and b_2 do not have clear theoretical meanings.

2.2 Data sources and pre-processing

The observed hourly concentrations of O_3, NO_2 and NO_x (2014-2019) for the regions of BTH, FWP, YRD, PRD and Hong Kong in China, as well as the US and EU were employed to investigate the parameterization of the DPO_3-NO_x (or NO_2) relation. Data were sourced from the Ministry of Ecology and Environment of the People's Republic of China (https://data.epmap.org), the Environmental Protection Department of Hong Kong (https://cd.epic.epd.gov.hk), the United States Environmental Protection Agency (https://aqs.epa.gov/aqsweb/airdata/download_files.html#Raw), and the European Environment Agency (discomap.eea.europa.eu/map/fme/AirQualityExport.htm), respectively. Only stations with more than 75% completeness of recordings per year or during the entire study were included in this study. For Macao, the data were obtained from the high-resolution Chinese air quality reanalysis dataset (CAQRA, 15 km) (https://www.scidb.cn/cstr/31253.11.sciencedb.00053). The pollutant concentration was expressed as mixing ratio (ppb).

In order to avoid the cleanup effects on the DPO_3-NO_x (or NO_2) relation caused by transport, ventilation and deposition, only the hours with calm wind (≤ 3.3 m/s) and "no precipitation" were incorporated. The hourly meteorological datasets used for pollution data screening included the National Oceanic and Atmospheric Administration (NOAA) Integrated Surface

Database (ISD) (ftp://ftp.ncdc.noaa.gov/pub/data/noaa/isd-lite), the CAQRA dataset, and the European Centre of Medium-range Weather Forecasts Reanalysis v.5 (ERA5) global reanalysis datasets (31 km) (https://www.ecmwf.int/en/forecasts/dataset/ecmwf-reanalysis-v5).

For the EU and US, the "no precipitation" scenario was defined as the hours of 50% cloud cover with the records ≤ 4 in ISD, rather than the zero-precipitation hours, due to the limited rainfall recordings in the ISD compared to cloud cover, especially in the US. The wind speed and cloud cover data for a specific pollutant station were derived from the recordings at its nearest surrounding ISD station(s) located within 15 km and 50 km, respectively. Pollution monitoring stations without matching meteorological information were excluded.

For the studied regions in China, the ISD recordings of both precipitation and cloud cover were sparse, and the number of meteorological stations were insufficient for regional representation (BTH: 11 stations, FWP: 9 stations, YRD: 29 stations, GBA: 5 stations). In order to retain as much data as possible, the windspeed and precipitation data were extracted from CAQRA and ERA5 datasets, respectively. The CAQRA gridded screening wind speed was adjusted from 3.3 m/s to 6 m/s, based on the linear regression relation between the ISD observation stations and their corresponding CAQRA gridded records. In these regions, the "no precipitation" scenario was exactly defined as the zero-precipitation (< 2mm) hours, based on the ERA5 gridded rainfall records. The data processes and visualization in this study were conducted with R and Python.

A total of 493 stations (14 in EU, 114 in US, 70 in BTH, 55 in FWP, 169 in YRD, 71 in GBA (57 in PRD, 14 in Hong Kong)), and 1 CAQRA grid (for Macao) were incorporated to compare the capabilities of different parametric models (Figure S1). A total of 1306, 813, 1814 and 305 CAQRA grids were respectively employed to investigate the spatiotemporal variations of O_3-NO_x-VOC sensitivity from 2014 to 2019 for the regions of BTH, FWP, YRD and CBA in China.

3 Results and discussion

3.1. The DPO_3−NO_x (or NO_2) relation is empirically validated worldwide.

Based on the non-parametric approach, almost all pollution monitoring stations (including the Macao grid) during 2014-2019 were able to be characterized as part of a theoretical DPO_3-NO_x (or NO_2) diagram corresponding to the Scenario A, B or C (Graphical Abstract), except three stations in US. This indicates that such a regular diagram is globally prevalent, even in regions with severe $PM_{2.5}$ contamination, where the ozone formation is additionally influenced by the aerosol-inhibited photochemical regime, such as BTH, FWP and YRD in China (Ivatt et al., 2022; Geng et al., 2021; Kong et al., 2021; Xiao et al., 2022a). Based on the seven studied models (Equations 1-7), the parametric fitting curves were generally consistent with their corresponding non-parametric smoothened curves on the regional scale (Figures S2-S10). To further investigate their global fitting capabilities, these models were individually applied to regress the DPO_3-NO_x (or NO_2) relation for all the studied stations and the Macao grid.

3.2 Which is the most capable parametric model?

All 494 parametric fits converged using the models of *log-Bragg3*, *log-Bragg4*, *log-Lorentz3* and *log-Lorentz4* (Equations 3-7). However, based on the *Beta* and *log-Beta* models (Equations 1-2), a total of 59 and 69 out of the 494 DPO_3-NO_2 fits failed to converge, respectively, for all studied stations; while 17 and 21 out of the 142 DPO_3-NO_x fits did not converge in Hong Kong, EU and US. Notably, not all the convergent fits were able to characterize a regular diagram to effectively partition O_3-NO_x-VOC sensitivity. The amounts of the convergent and effective fits varied across the studied models: *log-poly2* (142 out of 142 DPO_3-NO_x fits, 494 out of 494 DPO_3-NO_2 fits) > *log-Bragg3* (141/142, 490/494) > *log-Lorentz3* (141/142, 489/494) > *log-Bragg4* (140/142, 488/494) > *log-Lorentz4* (122/142, 419/494) > *log-Beta* (121/142, 425/494) > *Beta* (114/142, 405/494). Although all the *logarithmic Poly2* fits (Equation 7) were convergent and effective, quite certain portion of them did not achieve the statistical significance ($p > 0.1$) (Figures S11-S12 (g)). Amongst all models, the *log-Bragg3* and *log-Lorentz3* models performed the best, with over 95% of fits achieving the statistical significance ($p < 0.1$) (Figures S11-S12 (c, e)). Detailed comparisons of the models' fitting performances are provided in Supporting Information (Text S1).

By excluding all non-convergent and irregularly convergent fits, as well as fits corresponding to Scenario A or C as shown in Graphical Abstract (52 DPO_3-NO_2 fits and 18 DPO_3-NO_x fits), a total of 442 DPO_3-NO_2 fits and 124 DPO_3-NO_x fits were incorporated for comparing the partition points identified using the non-parametric and parametric approaches (Figure 1). For the DPO_3-NO_2 relation (Figure 1 (a-g)), the *Beta*, *log-Beta*, *log-Bragg3*, *log-Bragg4*, and *log-Lorentz3* models show strong alignment ($r^2 \geqslant 94\%$, slopes: 0.84-0.89) (Figure 1 (a-e)). However, only the *log-Bragg3* and *log-Lorentz3* models (Figure 1 (c, e)) identified the partition points for all fits under Scenario B (Graphical Abstract). Similarly, for the DPO_3-NO_x relation, these two models (Figure 1 (j, l)) also exhibit the best performances.

Despite comparable performance in terms of amounts of convergent and effective fits, fitting statistical significance, and ability to identify partition point between the *log-Bragg3* and *log-Lorentz3* models, the *log-Bragg3* model is preferred due to the generally inferior statistical properties exhibited by *Lorentz* models (Ratkowsky, 1990).

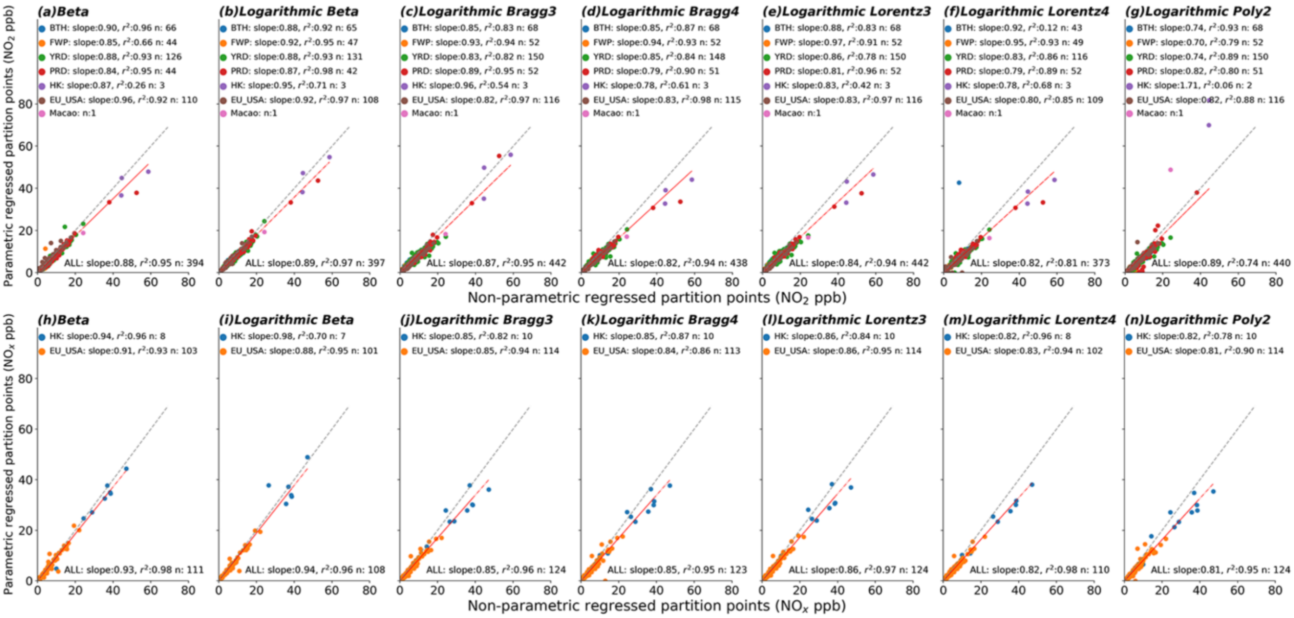

Figure 1: Comparisons of the partition points recognized between the parametric (y-axis) and non-parametric (x-axis) approaches based on the DPO_3-NO_2 (a-g) and DPO_3-NO_x (h-n) relations, respectively.

3.3 Comparison of reliabilities between the DPO_3-NO_2 and DPO_3-NO_x curves

The proportion of data points with NO_x (or NO_2) concentrations on the right of the partition points (referred to as VOC-limited % below) correlated well between the *log-Bragg3* model and the non-parametric method for both DPO_3-NO_2 and DPO_3-NO_x curves (Figure 2 (a, b)). Notably, the agreement on DPO_3-NO_2 partition points was poor in Hong Kong (Figure 1 (c)), while it was improved for DPO_3-NO_x relation (Figure 1 (j)). Most DPO_3-NO_x fits (n=10) in Hong Kong aligned with Scenario B, featuring a clear partition point, whereas most DPO_3-NO_2 fits (n=8) corresponded to Scenario A (Graphical Abstract). This confirms differing performances of these two curves in diagnosing O_3-NO_x-VOC sensitivity. Fortunately, the VOC-limited % derived from both DPO_3-NO_2 and DPO_3-NO_x curves agreed well across EU and US; and only some stations in Hong Kong showed the conflicting results: a VOC-limited regime (VOC-limited % > 50%) based on DPO_3-NO_x fit v.s. a NO_x-limited/transition regime (VOC-limited % = 0) based on DPO_3-NO_2 fit (Figure 2 (c, d)).

The DPO_3/NO_2 ratios at these stations in Hong Kong ranged from 0.1 to 0.6, much lower than other stations/grid (BTH: 1.1-4.0, FWP: 1.3-3.4, YRD: 1.4-4.5, PRD: 1.3-4.5, Macao: 2.1, EU_US: 0.3-16.5, other stations in Hong Kong: 0.8-6.5). A low DPO_3/NO_2 ratio typically indicates a condition that the reaction of OH with NO_2 dominates the fate of HO_x, slowing the oxidation of organic precursor, and gradually terminating the ozone production (Pusede et al., 2015; Romer et al., 2018). The ozone production decreases with NO_2 under this condition, leading to a pseudo diagnostic result indicative of a NO_x-limited regime under a realistic NO_x-saturated condition (Guo et al., 2023; Romer et al., 2018; Pusede et al., 2015). Hence, the DPO_3-

NO_x curve is considered more reliable for diagnosing O_3-NO_x-VOC sensitivity at any NO_x level, and it is recommended to check the DPO_3/NO_2 ratio before employing the DPO_3-NO_2 curve.

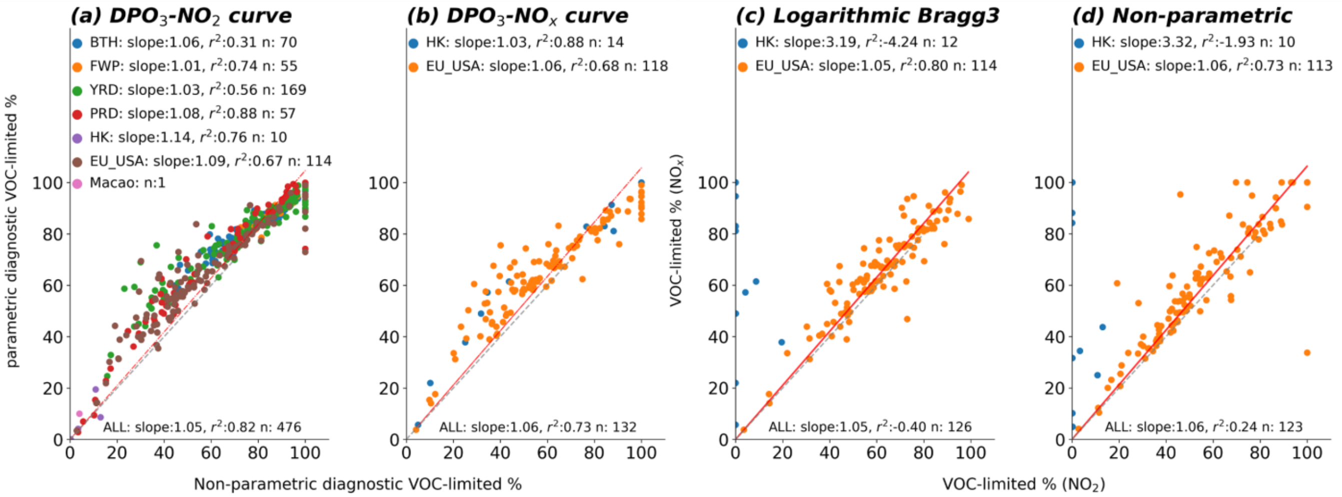

Figure 2: Comparisons of the VOC-limited % diagnosed between the *log-Bragg3* model (y-axis) and non-parametric approach (x-axis) based on the DPO_3-NO_2 (a) and DPO_3-NO_x (b) relations, respectively, and between the DPO_3-NO_2 (y-axis) and DPO_3-NO_x (x-axis) fits with the *log-Bragg3* model (c) and non-parametric approach (d), respectively.

3.4 The O_3-NO_x-VOC sensitivity evolution on the regional scale

The evolution of O_3-NO_x-VOC sensitivity (or OFR) was diagnosed based on the variations in the DPO_3-NO_2 curves between 2014 and 2019 using the *logarithmic Bragg 3* model (Figures 3 and S13). The O_3-NO_x-VOC sensitivity (or OFR) for a specific region/station/grid was diagnosed as a NO_x-limited regime, transition regime and VOC-limited regime, if the average NO_2 concentration was lower than the transition point, between the transition and partition points, and higher than the partition point, respectively. The parametric partition point corresponded to the parameter *e*. The parametric transition point (blue dotted line in Figures 3 and S13) was defined as the NO_2 level at the maximum slope midpoint of fitting curve, corresponding to DPO_3 level in the top 4.9% of *log-Bragg3* model predictions. The non-parametric transition point was determined as the NO_2 level corresponding to the top 4.9% smoothing DPO_3 level (red dotted line in Figures 3 and S13).

The observed regional DPO_3/NO_2 ratios were 1.78, 1.63, 2.18, 1.77 and 3.86 (EU: 0.88, US: 4.03) for BTH, FWP, YRD, GBA and EU/US in 2014, and increased to 2.49, 2.45, 2.71, 2.33 and 4.77 (EU: 1.05, US: 4.98) in 2019, respectively. These generally median ratio levels suggest that the DPO_3-NO_2 curve is likely to effectively diagnose the OFR evolution on the regional/national scale. All studied regions were consistently under the VOC-limited regime in both years. However, it is noteworthy that the annual VOC-limited % in BTH, FWP, GBA, EU and US experienced varying declines from 2014 to 2019 (Table S1). This trend of OFR evolving to a less NO_x-saturated condition in recent years has also been reported for other city clusters worldwide (Vazquez Santiago et al., 2024). Conversely, the YRD region showed a slight shift towards more NO_x-

https://doi.org/10.5194/egusphere-2025-1596
Preprint. Discussion started: 29 April 2025

saturated from 2014 (annual VOC-limited %: 72.10 %) to 2019 (84.63 %), despite a decline in its average NO_2 level; this could be attributed to a more pronounced decline in partition point (Figure 3 (c, h), Table S1), resulting in more scenarios falling to the right of the partition point in 2019. The CAQRA gridded data-based regional diagnosis showed the similar results for the four Chinese city agglomerations (Figure S13, Table S2).

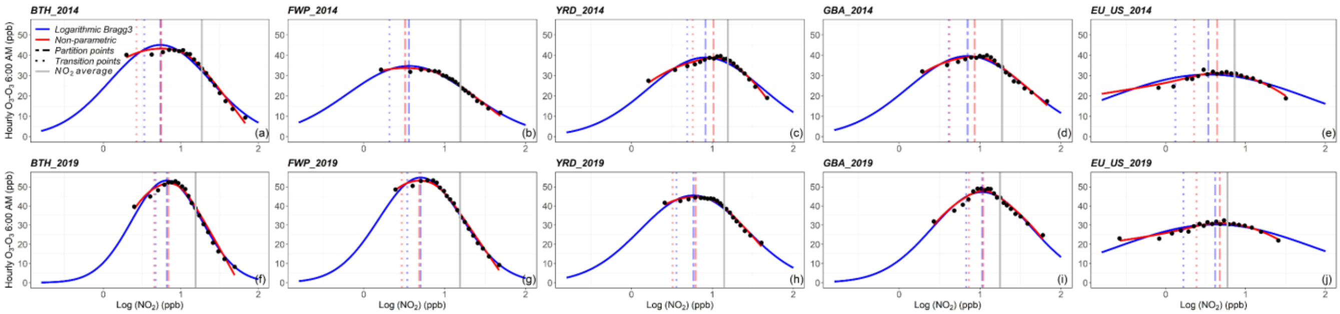

Figure 3: Variations of the DPO_3-NO_2 curves from 2014 (a-e) to 2019 (f-j) on the regional scale based on the observation data. The diagnostic results for both EU and US agreed well between the DPO_3-NO_2 and DPO_3-NO_x fits, so their DPO_3-NO_x curves were not additionally provided.

3.5 Implications of the *log-Bragg 3* model's parameters (*b*, *d*)

Based on the observation data, the parameter *d*, that represents the maximum DPO_3, exhibited higher for the studied regions in China compared with the EU/ US; additionally, the parameter *b* in China was consistently higher in 2019 compared to 2014 (Table S1). This indicates that the regional ozone production in China was more intense and the ozone pollution deteriorated from 2014 to 2019, consistent with the findings in previous studies (Lu et al., 2018; Lu et al., 2020). In theory, at low NO_x level, increasing NO enhances the reactions of RO_2+NO and HO_2+NO, thereby promoting ozone production (Equation 8). As NO_x increases, the NO_x consumption (Equations 9-10) gradually rises, leading to a reduction in ozone production efficiency. At high NO_x level, the production of HNO_3 (Equation 10), accelerates significantly and constitutes the predominant NO_x consumption pathway and HO fate, thereby gradually suppressing ozone production (Romer et al., 2018; Pusede et al., 2015; Farmer et al., 2011). The higher value of parameter *b* observed in China, compared with the EU/US (Table S1), characterizes a steeper curve, and indicates a faster change in ozone production efficiency for a given increment of NO_x. In addition, the distinct trends in temporal variation of parameter *b* between the regions in China (increasing from 2014 to 2019) and EU/ US (decreasing from 2014 to 2019) (Table S1) imply that they were experiencing different variations in ozone formation chemistry.

$$PO_3 = (1-\alpha)k_{NO+RO_2}[NO][RO_2] + k_{NO+HO_2}[NO][HO_2] \quad \text{(Equation 8)}$$

$$P\sum RONO_2 = \alpha k_{NO+RO_2}[NO][RO_2] \quad \text{(Equation 9)}$$

$$PHNO_3 = k_{OH+NO_2}[OH][NO_2] \quad \text{(Equation 10)}$$

3.6 Spatiotemporal variation diagnosis of O_3-NO_x-VOC sensitivity and associated uncertainty

In BTH and FWP, almost all stations and grids were diagnosed as being under the VOC-limited regime in both 2014 and 2019; in most areas of YRD and GBA, the ozone formation were also sensitive to VOC, except those tiny coastal zones (Figure S14). The VOC-limited areas diagnosed in our study were much dominant than those recognized using the satellite-derived $HCHO/NO_2$ ratio (FNR)-based method (Jin and Holloway, 2015; Wang et al., 2021; Ren et al., 2022; Zhang et al., 2024). This discrepancy can be attributed to the differences in studied periods and daily hours, as well as the bias in the satellite-based method. On one hand, our study focused on the entire year and MDA8-daytime hours, while the satellite-based studies covered the ozone-season midday (13:00-14:00 LT), when higher temperatures make ozone formation more NO_x-sensitive (Pusede et al., 2014; Pusede et al., 2015; Yang et al., 2021; Huang et al., 2025).This can be further supported by the ozone-season midday (April-September, 13:00-14:00 LT) specific diagnostic results as shown in Figure S15, in which the VOC-limited areas were notably reduced for BTH, YRD and GBA. The satellite-derived column FNR is likely to represent the average condition within the column height, rather than the near-surface condition. The concentrations of ozone and its precursors, as well as the FNRs, vary with heights (Liao et al., 2021; Mo et al., 2022; Li et al., 2024; Li et al., 2020), and the near-surface environment had been reported to be more VOC-limited (Li et al., 2024). Furthermore, the satellite-derived HCHO cannot differentiate the primary emitted and secondary produced HCHO, whereas the latter is more indicative of the VOC reactions (Liu et al., 2021). Therefore, the satellite-based method is likely to overestimate the near-surface condition, leading to some VOC-limited conditions being misdiagnosed as in the NO_x-limited or transition regime.

Beyond Hong Kong, the DPO_3-NO_2 pseudo-diagnosis was also explicitly identified at some stations in BTH and YRD, highlighted with red circles in Figure 4. The VOC-limited % were recognized near zero (e.g., < 0.1 %) at those stations with the DPO_3/NO_2 ratios from 0.31 to 0.84 in 2014; and increased to above 65% with the notably higher ratios (1.91-3.17) in 2019. As discussed before, the DPO_3-NO_2 curve is effective for OFR diagnosis only if the DPO_3/NO_2 ratio is not too low. However, it is difficult to figure out the threshold for the “lowest” ratio, as it varies with studied periods and sites. For instance, the DPO_3-NO_2 curve could still be reasonably applied at some stations in YRD in 2014, where the DPO_3/NO_2 ratios and the diagnostic VOC-limited % ranged from 0.36 to 0.78 and from 80% to 100%, respectively. Fortunately, such pseudo-diagnosis was not found for either the stations or grids in both FWP and PRD (Figures 4 (d-f, j-l) and S14 (c-d, g-h)). The spatiotemporal diagnostic results in Hong Kong were based on the DPO_3-NO_x curve.

The VOC-limited % for most areas in FWP experienced varying declines from 2014 to 2019 (Figure 4 (d-f)). For GBA, the areas with the highest VOC-limited % in 2014 were located along the cities from the eastern Pearl River Estuary (PRE) to the northwest of the Bay Area, where the VOC-limited % declined the most by 2019; conversely, the VOC-limited % increased in the surrounding areas that were originally more NO_x-limited in 2014, especially in the northern and eastern areas (Figure 5 (j-l)). 265

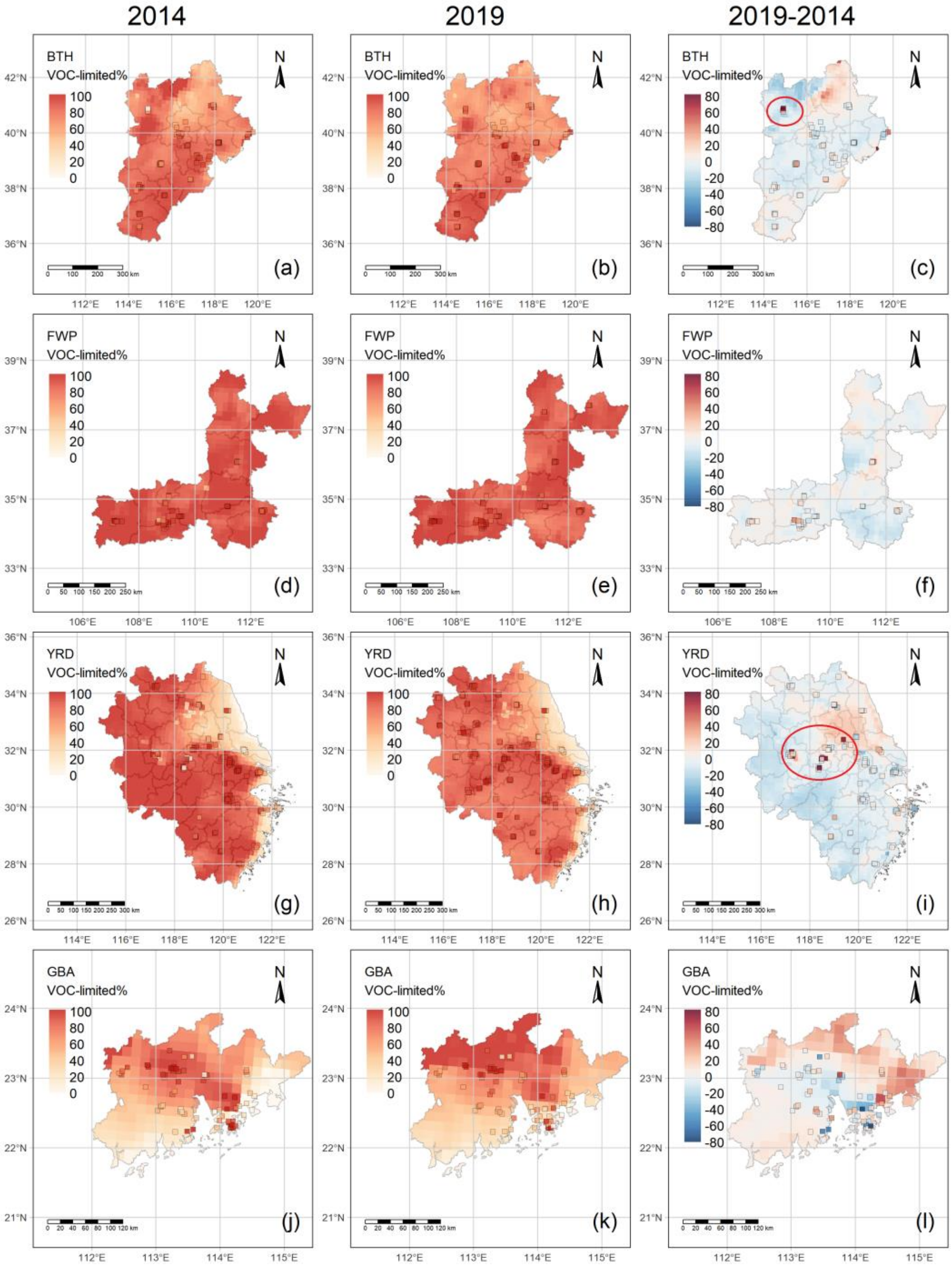

Figure 4: Spatiotemporal variations of the VOC-limited % from 2014 to 2019 in four city agglomerations of China, based on the *logarithmic Bragg 3* model fitting DPO_3-NO_2 curves.

4. Conclusion

The identified empirical model, *log-Bragg3* model (Equation 3), adaptably resolves the O_3-NO_x-VOC sensitivity continuum, and provide parametric insights into ozone formation intensity (d), associated chemical processes (b), and the O_3-NO_x-VOC sensitivity partition threshold (e). More vigorous photochemical reactions are implicated in the studied Chinese regions by higher values of parameters b and d relative to EU/US. Divergent temporal trends in parameter b further indicate fundamentally distinct evolutionary pathways in regional ozone chemistry between China and western regions. Compared with previous satellite-derived FNR-based studies, our diagnostic results demonstrated a higher prevalence of VOC-limited regimes. This is because our findings reflect the near-surface conditions specific to MDA8 daytime hours throughout an entire year, rather than the average conditions within the satellite column at midday during the ozone season. This parametric methodology overcomes the complexities and resource constraints inherent in conventional methods, and is expected as a unified tool to facilitate global ozone mitigation under evolving precursor emission patterns and climate change. However, the DPO_3-NO_2 curve-based pseudo-diagnosis can introduce significant uncertainty in cases of extremely low DPO_3/NO_2 ratio. In contrast, the DPO_3-NO_x curve demonstrates superior reliability and is recommended for future studies.

Supplement

Comparison of fitting significance amongst parametric models (Text S1); locations of the studied pollution monitoring stations (Figure S1); the DPO_3-NO_2 curves for BTH, FWP, YRD, PRD, Hong Kong, Macao and EU_US (2014-2019) individually fitted by the studied models (Figures S2-S6 and S8-S9); the DPO_3-NO_x curves for Hong Kong and EU_US (2014-2019) individually fitted by the studied models (Figures S7 and S10); the *p*-values per parameters in the convergent and effective DPO_3-NO_x (or NO_2) fits based on the studied models (Figures S11-S12); variations of the DPO_3-NO_2 curves from 2014 to 2019 on the regional scale based on the CAQRA gridded data (Figure S13); spatiotemporal variations of the all-year MDA8-daytime-hour- and ozone-season midday specific ozone formation regimes (OFRs) from 2014 to 2019 in four city agglomerations of China based on the *log-Bragg 3* model fitting DPO_3-NO_2 curves (Figures S14-S15); the fitting parameters, average levels (ppb) of NO_2 and DPO_3, partition points (ppb), transition points (ppb), as well as the proportions (%) respectively under the VOC-limited, transition and NOx-limited regimes specific to Figure 3 and Figure S13 (Tables S1 and S2).

Author contributions

MH conceived and designed the research, collected and processed the data, developed the R code for the DPO_3-NO_x (or NO_2) curve regression and O_3-NO_x-VOC sensitivity diagnosis, and drafted the manuscript; TL collected and processed the data, performed statistical analyses, and visualized the results.

Code availability

The data processes and visualization were conducted with R and Python, and the relevant code can be obtained upon request to the corresponding author.

Data availability

The original data sources are detailed in Section 2.2, and the input data for figure visualization can be provided upon request to the corresponding author.

Competing interests

The authors declare no competing financial interest.

Acknowledgments

The authors sincerely acknowledge Dr. Haichao Wang from School of Atmospheric Sciences at Sun Yat-sen University, PR China, for his insights regarding the vertical variations of pollutants, which inspired us to give the possible reasons for the discrepancy between our diagnostic results and the previous satellite-derived FNR-based results.

References

Agathokleous, E., Sicard, P., Feng, Z., and Paoletti, E.: Ozone pollution threatens bird populations to collapse: an imminent ecological threat?, Journal of Forestry Research, 34, 1653-1656, 10.1007/s11676-023-01645-y, 2023.

Agathokleous, E., Feng, Z., Oksanen, E., Sicard, P., Wang, Q., Saitanis, C. J., Araminiene, V., Blande, J. D., Hayes, F., Calatayud, V., Domingos, M., Veresoglou, S. D., Peñuelas, J., Wardle, D. A., De Marco, A., Li, Z., Harmens, H., Yuan, X., Vitale, M., and Paoletti, E.: Ozone affects plant, insect, and soil microbial communities: A threat to terrestrial ecosystems and biodiversity, Science Advances, 6, eabc1176, doi:10.1126/sciadv.abc1176, 2020.

Atkinson, R.: Atmospheric chemistry of VOCs and NOx, Atmospheric Environment, 34, 2063-2101, https://doi.org/10.1016/S1352-2310(99)00460-4, 2000.

Ban, J., Lu, K., Wang, Q., and Li, T.: Climate change will amplify the inequitable exposure to compound heatwave and ozone pollution, One Earth, 5, 677-686, https://doi.org/10.1016/j.oneear.2022.05.007, 2022.

Collaborators, G. R. F.: Global burden of 87 risk factors in 204 countries and territories, 1990-2019: a systematic analysis for the Global Burden of Disease Study 2019, Lancet, 396, 1223-1249, 10.1016/s0140-6736(20)30752-2, 2020.

Farmer, D. K., Perring, A. E., Wooldridge, P. J., Blake, D. R., Baker, A., Meinardi, S., Huey, L. G., Tanner, D., Vargas, O., and Cohen, R. C.: Impact of organic nitrates on urban ozone production, Atmos. Chem. Phys., 11, 4085-4094, 10.5194/acp-11-4085-2011, 2011.

Feng, Z., Xu, Y., Kobayashi, K., Dai, L., Zhang, T., Agathokleous, E., Calatayud, V., Paoletti, E., Mukherjee, A., Agrawal, M., Park, R. J., Oak, Y. J., and Yue, X.: Ozone pollution threatens the production of major staple crops in East Asia, Nature Food, 3, 47-56, 10.1038/s43016-021-00422-6, 2022.

Geng, G., Xiao, Q., Liu, S., Liu, X., Cheng, J., Zheng, Y., Xue, T., Tong, D., Zheng, B., Peng, Y., Huang, X., He, K., and Zhang, Q.: Tracking Air Pollution in China: Near Real-Time PM2.5 Retrievals from Multisource Data Fusion, Environmental Science & Technology, 55, 12106-12115, 10.1021/acs.est.1c01863, 2021.

Guo, J., Zhang, X., Gao, Y., Wang, Z., Zhang, M., Xue, W., Herrmann, H., Brasseur, G. P., Wang, T., and Wang, Z.: Evolution of Ozone Pollution in China: What Track Will It Follow?, Environmental Science & Technology, 57, 109-117, 10.1021/acs.est.2c08205, 2023.

Huang, M., Feng, Z., and Liao, T.: Shift of surface O3-NOx-VOC sensitivity with temperature in the Guangdong-Hong Kong-Macao Greater Bay Area, South China, Environmental Pollution, 125974, https://doi.org/10.1016/j.envpol.2025.125974, 2025.

Ivatt, P., Evans, M., and Lewis, A.: Suppression of surface ozone by an aerosol-inhibited photochemical ozone regime, Nature Geoscience, 15, 1-5, 10.1038/s41561-022-00972-9, 2022.

Jin, X. and Holloway, T.: Spatial and temporal variability of ozone sensitivity over China observed from the Ozone Monitoring Instrument, Journal of Geophysical Research: Atmospheres, 120, 7229-7246, https://doi.org/10.1002/2015JD023250, 2015.

Kong, L., Tang, X., Zhu, J., Wang, Z., Li, J., Wu, H., Wu, Q., Chen, H., Zhu, L., Wang, W., Liu, B., Wang, Q., Chen, D., Pan, Y., Song, T., Li, F., Zheng, H., Jia, G., Lu, M., Wu, L., and Carmichael, G. R.: A 6-year-long (2013–2018) high-resolution air quality reanalysis dataset in China based on the assimilation of surface observations from CNEMC, Earth Syst. Sci. Data, 13, 529-570, 10.5194/essd-13-529-2021, 2021.

Li, K., Jacob, D. J., Liao, H., Zhu, J., Shah, V., Shen, L., Bates, K. H., Zhang, Q., and Zhai, S.: A two-pollutant strategy for improving ozone and particulate air quality in China, Nature Geoscience, 12, 906-910, 10.1038/s41561-019-0464-x, 2019.

Li, L., Lu, C., Chan, P.-W., Zhang, X., Yang, H.-L., Lan, Z.-J., Zhang, W.-H., Liu, Y.-W., Pan, L., and Zhang, L.: Tower observed vertical distribution of PM2.5, O3 and NOx in the Pearl River Delta, Atmospheric Environment, 220, 117083, https://doi.org/10.1016/j.atmosenv.2019.117083, 2020.

Li, Q., Zhang, L., Wang, T., Wang, Z., Fu, X., and Zhang, Q.: “New” Reactive Nitrogen Chemistry Reshapes the Relationship of Ozone to Its Precursors, Environmental Science & Technology, 52, 2810-2818, 10.1021/acs.est.7b05771, 2018.

Li, Y., Xing, C., Hong, Q., Jiao, P., Peng, H., Tang, Z., and Liu, C.: Ozone Formation Sensitivity at Various Altitudes: Seeking the Optimal Method for Sensitivity Threshold Determination, Environmental Science & Technology Letters, 11, 1334-1339, 10.1021/acs.estlett.4c00777, 2024.

https://doi.org/10.5194/egusphere-2025-1596
Preprint. Discussion started: 29 April 2025

Liao, Z., Ling, Z., Gao, M., Sun, J., Zhao, W., Ma, P., Quan, J., and Fan, S.: Tropospheric Ozone Variability Over Hong Kong Based on Recent 20 years (2000–2019) Ozonesonde Observation, Journal of Geophysical Research: Atmospheres, 126, e2020JD033054, https://doi.org/10.1029/2020JD033054, 2021.

Liu, J., Li, X., Tan, Z., Wang, W., Yang, Y., Zhu, Y., Yang, S., Song, M., Chen, S., Wang, H., Lu, K., Zeng, L., and Zhang, Y.: Assessing the Ratios of Formaldehyde and Glyoxal to NO2 as Indicators of O3–NOx–VOC Sensitivity, Environmental Science & Technology, 55, 10935-10945, 10.1021/acs.est.0c07506, 2021.

Lu, X., Zhang, L., Wang, X., Gao, M., Li, K., Zhang, Y., Yue, X., and Zhang, Y.: Rapid Increases in Warm-Season Surface Ozone and Resulting Health Impact in China Since 2013, Environmental Science & Technology Letters, 7, 240-247, 10.1021/acs.estlett.0c00171, 2020.

Lu, X., Hong, J., Zhang, L., Cooper, O. R., Schultz, M. G., Xu, X., Wang, T., Gao, M., Zhao, Y., and Zhang, Y.: Severe Surface Ozone Pollution in China: A Global Perspective, Environmental Science & Technology Letters, 5, 487-494, 10.1021/acs.estlett.8b00366, 2018.

Mo, Z., Huang, S., Yuan, B., Pei, C., Song, Q., Qi, J., Wang, M., Wang, B., Wang, C., and Shao, M.: Tower-based measurements of NMHCs and OVOCs in the Pearl River Delta: Vertical distribution, source analysis and chemical reactivity, Environmental Pollution, 292, 118454, https://doi.org/10.1016/j.envpol.2021.118454, 2022.

Nussbaumer, C. M. and Cohen, R. C.: The Role of Temperature and NOx in Ozone Trends in the Los Angeles Basin, Environmental Science & Technology, 54, 15652-15659, 10.1021/acs.est.0c04910, 2020.

Ou, J., Yuan, Z., Zheng, J., Huang, Z., Shao, M., Li, Z., Huang, X., Guo, H., and Louie, P. K. K.: Ambient Ozone Control in a Photochemically Active Region: Short-Term Despiking or Long-Term Attainment?, Environmental Science & Technology, 50, 5720-5728, 10.1021/acs.est.6b00345, 2016.

Pusede, S. E. and Cohen, R. C.: On the observed response of ozone to NO_x and VOC reactivity reductions in San Joaquin Valley California 1995–present, Atmos. Chem. Phys., 12, 8323-8339, 10.5194/acp-12-8323-2012, 2012.

Pusede, S. E., Steiner, A. L., and Cohen, R. C.: Temperature and Recent Trends in the Chemistry of Continental Surface Ozone, Chemical Reviews, 115, 3898-3918, 10.1021/cr5006815, 2015.

Pusede, S. E., Gentner, D. R., Wooldridge, P. J., Browne, E. C., Rollins, A. W., Min, K. E., Russell, A. R., Thomas, J., Zhang, L., Brune, W. H., Henry, S. B., DiGangi, J. P., Keutsch, F. N., Harrold, S. A., Thornton, J. A., Beaver, M. R., St. Clair, J. M., Wennberg, P. O., Sanders, J., Ren, X., VandenBoer, T. C., Markovic, M. Z., Guha, A., Weber, R., Goldstein, A. H., and Cohen, R. C.: On the temperature dependence of organic reactivity, nitrogen oxides, ozone production, and the impact of emission controls in San Joaquin Valley, California, Atmos. Chem. Phys., 14, 3373-3395, 10.5194/acp-14-3373-2014, 2014.

Ratkowsky, D. A.: Ratkowsky, D.A., 1990. Handbook of nonlinear regression models, Marcel Dekker Inc., New York, USA.1990.

Ren, J., Guo, F., and Xie, S.: Diagnosing ozone–NOx–VOC sensitivity and revealing causes of ozone increases in China based on 2013–2021 satellite retrievals, Atmos. Chem. Phys., 22, 15035-15047, 10.5194/acp-22-15035-2022, 2022.

Romer, P. S., Duffey, K. C., Wooldridge, P. J., Edgerton, E., Baumann, K., Feiner, P. A., Miller, D. O., Brune, W. H., Koss, A. R., de Gouw, J. A., Misztal, P. K., Goldstein, A. H., and Cohen, R. C.: Effects of temperature-dependent NOx emissions on continental ozone production, Atmos. Chem. Phys., 18, 2601-2614, 10.5194/acp-18-2601-2018, 2018.

Schnell, J. L. and Prather, M. J.: Co-occurrence of extremes in surface ozone, particulate matter, and temperature over eastern North America, Proceedings of the National Academy of Sciences, 114, 2854-2859, doi:10.1073/pnas.1614453114, 2017.

Sillman, S. and He, D.: Some theoretical results concerning O3-NOx-VOC chemistry and NOx-VOC indicators, Journal of Geophysical Research: Atmospheres, 107, ACH 26-21-ACH 26-15, https://doi.org/10.1029/2001JD001123, 2002.

Sillman, S. and West, J. J.: Reactive nitrogen in Mexico City and its relation to ozone-precursor sensitivity: results from photochemical models, Atmos. Chem. Phys., 9, 3477-3489, 10.5194/acp-9-3477-2009, 2009.

Vazquez Santiago, J., Hata, H., Martinez-Noriega, E. J., and Inoue, K.: Ozone trends and their sensitivity in global megacities under the warming climate, Nature Communications, 15, 10236, 10.1038/s41467-024-54490-w, 2024.

Wang, H., Lu, X., Palmer, P. I., Zhang, L., Lu, K., Li, K., Nagashima, T., Koo, J.-H., Tanimoto, H., Wang, H., Gao, M., He, C., Wu, K., Fan, S., and Zhang, Y.: Deciphering decadal urban ozone trends from historical records since 1980, National Science Review, 11, 10.1093/nsr/nwae369, 2024.

Wang, T., Xue, L., Brimblecombe, P., Lam, Y. F., Li, L., and Zhang, L.: Ozone pollution in China: A review of concentrations, meteorological influences, chemical precursors, and effects, Science of The Total Environment, 575, 1582-1596, https://doi.org/10.1016/j.scitotenv.2016.10.081, 2017.

Wang, W., van der A, R., Ding, J., van Weele, M., and Cheng, T.: Spatial and temporal changes of the ozone sensitivity in China based on satellite and ground-based observations, Atmos. Chem. Phys., 21, 7253-7269, 10.5194/acp-21-7253-2021, 2021.

Xiao, Q., Geng, G., Liu, S., Liu, J., Meng, X., and Zhang, Q.: Spatiotemporal continuous estimates of daily 1 km PM2.5 from 2000 to present under the Tracking Air Pollution in China (TAP) framework, Atmos. Chem. Phys., 22, 13229-13242, 10.5194/acp-22-13229-2022, 2022a.

Xiao, X., Xu, Y., Zhang, X., Wang, F., Lu, X., Cai, Z., Brasseur, G., and Gao, M.: Amplified Upward Trend of the Joint Occurrences of Heat and Ozone Extremes in China over 2013–20, Bulletin of the American Meteorological Society, 103, E1330-E1342, https://doi.org/10.1175/BAMS-D-21-0222.1, 2022b.

Xue, L., Wang, T., Louie, P. K. K., Luk, C. W. Y., Blake, D. R., and Xu, Z.: Increasing External Effects Negate Local Efforts to Control Ozone Air Pollution: A Case Study of Hong Kong and Implications for Other Chinese Cities, Environmental Science & Technology, 48, 10769-10775, 10.1021/es503278g, 2014.

Yang, L., Yuan, Z., Luo, H., Wang, Y., Xu, Y., Duan, Y., and Fu, Q.: Identification of long-term evolution of ozone sensitivity to precursors based on two-dimensional mutual verification, Science of The Total Environment, 760, 143401, https://doi.org/10.1016/j.scitotenv.2020.143401, 2021.

Zhang, J., Shen, A., Jin, Y., Cui, Y., Xu, Y., Lu, X., Liu, Y., and Fan, Q.: Evolution of ozone formation regimes during different periods in representative regions of China, Atmospheric Environment, 338, 120830, https://doi.org/10.1016/j.atmosenv.2024.120830, 2024.

Zhang, Q., Yin, Z., Lu, X., Gong, J., Lei, Y., Cai, B., Cai, C., Chai, Q., Chen, H., Dai, H., Dong, Z., Geng, G., Guan, D., Hu, J., Huang, C., Kang, J., Li, T., Li, W., Lin, Y., Liu, J., Liu, X., Liu, Z., Ma, J., Shen, G., Tong, D., Wang, X., Wang, X., Wang, Z., Xie, Y., Xu, H., Xue, T., Zhang, B., Zhang, D., Zhang, S., Zhang, S., Zhang, X., Zheng, B., Zheng, Y., Zhu, T., Wang, J., and He, K.: Synergetic roadmap of carbon neutrality and clean air for China, Environmental Science and Ecotechnology, 16, 100280, https://doi.org/10.1016/j.ese.2023.100280, 2023.